RSC Advances

PAPER

View Article Online
View Journal | View Issue

Cite this: *RSC Adv.*, 2021, **11**, 26800

Sunlight-assisted degradation of textile pollutants and phytotoxicity evaluation using mesoporous ZnO/g-C_3N_4 catalyst†

H. Leelavathi,[a] N. Abirami,[a] R. Muralidharan,[b] Helen P. Kavitha,[c] S. Tamizharasan,[a] S. Sankeetha[a] and R. Arulmozhi *[a]

Accessibility of adequate safe and fresh water for human consumption is one of the most significant issues throughout the world and extensive research is being undertaken to resolve it. Nanotechnology is now an outstanding medium for water treatment and remediation from microorganisms and organic dyes, as compared to conventional treatment methods. For this task graphitic carbon nitride (g-C_3N_4) is a potential nanomaterial for environmental remediation, but its photogenerated charge carrier recombination rate restricts its use in practical applications. Hence, in the current study, we used a simple one-step calcination method to synthesize various ratios of ZnO/g-C_3N_4 binary nanocomposites. The band gap of g-C_3N_4 is 2.70 eV, but it is shifted to 2.60 eV by the 0.75 : 1 ZnO/g-C_3N_4 binary nanocomposite. Moreover, phase structure, morphology, thermal stability, oxidation state, elemental analysis, and surface area were evaluated using XRD, SEM, TEM, TGA, XPS, and BET analysis. The optimal ZnO loading content was determined and the mechanism of enhanced photocatalytic activity was studied in detail. The photocatalytic efficiency of the best catalyst was employed for the degradation of textile effluent followed by phytotoxicity evaluation using methylene blue (MB), and rhodamine B (RhB) as a model substrate was tested. Furthermore, the textile effluent treatment analysis discovered that the 75 mg concentration of 0.75 : 1 ZnO/g-C_3N_4 catalyst degraded up to 80% within 120 min and significantly reduced the concentrations of different physico-chemical parameters of textile effluents. These treated effluents have no phytotoxic effects on fenugreek plants, according to a pot study. It was found that the mesoporous 0.75 : 1 ZnO/g-C_3N_4 catalyst can be used as an effective and low-cost technique for the degradation of azo dyes in textile wastewaters.

Received 15th May 2021
Accepted 28th July 2021

DOI: 10.1039/d1ra03806k

rsc.li/rsc-advances

1. Introduction

Water is essential for our day-to-day activities; however, water shortages and pollution have become critical targets for governments, industries, and civil society around the world as a result of rapid industrialization and population growth in recent decades.[1–3] According to the United Nations World Water Development Report, nearly 748 million people have been unaware of the scarcity of pure drinking water and since the turn of the 21st century, the amount of water needed by manufacturing industries will increase by 400 percent by 2050.[4,5] As a result, among the various types of contamination, there is an urgent need to establish reliable, dependable, and economically viable methods to deal with emerging water pollutants and resolve the safety problems caused by them, according to various researchers and scientists around the world.[6–9] Dye wastewater is one of the leading harmful industrial wastewaters that have been released from various industries, such as paints, textiles, printing inks, paper, plastic, and food.[10,11] Dye contamination contains a variety of biologically toxic and carcinogenic organic substances;[12,13] this causes serious environmental problems that affect human health and aquatic species. Because of their complex aromatic structure, most dyes cannot be degraded. Until now, many strategies like adsorption, catalytic degradation, biodegradation, flocculation, coagulation, sedimentation, and membrane filtration have been suggested as methods for removing water contaminants.[14–16] Photocatalytic degradation is widely regarded as one of the most cost-effective and environmentally sustainable methods among them. It involves transforming light energy into chemical energy through photocatalysts, which produce free radical groups, which then oxidize organic effluents into harmless substances.[17]

[a]*Department of Chemistry, SRM Institute of Science and Technology, Kattankulathur, 603203, Tamil Nadu, India*

[b]*Department of Physics, Vel Tech High Tech Dr Rangarajan Dr Sakunthala Engineering College, Avadi, Chennai, 600 062, Tamil Nadu, India*

[c]*Department of Chemistry, SRM Institute of Science and Technology, Ramapuram Campus, Chennai, 600 089, Tamil Nadu, India. E-mail: arulmozr@srmist.edu.in*

† Electronic supplementary information (ESI) available. See DOI: 10.1039/d1ra03806k

Due to the possible application of nanomaterials, the development of solar light active photocatalysts has sparked a lot of interest in recent years. Many dangerous organic compounds in wastewater can be degraded using photocatalysts that are activated by sunlight.[18–21] Graphitic carbon nitride (g-C_3N_4), a novel polymeric semiconductor, has recently attracted much interest as a potential material for organic pollution degradation and hydrogen generation through water splitting.[22,23] Being low cost and nontoxic, and having chemical and high thermal stability and a sufficient energy bandgap E_g (2.7 eV) are a few of the benefits of this material.[24] Coupling g-C_3N_4 with appropriate semiconductor metal oxides (ZnO, Fe_2O_3, Cu_2O, TiO_2, SnO_2, $BiVO_4$, NiO, WO_3, and ZrO_2) is another efficient method for developing sunlight active photocatalysts.[25] One of the most crucial factors in promoting efficient photoinduced charge transfer and separation, as well as reducing fast recombination, is selecting the right semiconductor photocatalyst with the right CB and VB potentials. Because of their high redox potential of photoinduced charge carriers, photocatalytic materials with a wider band gap, such as TiO_2 and ZnO, are already known to be reliable. In contrast to TiO_2, n-type ZnO semiconductors have recently gained popularity due to their low cost, environmental friendliness, simple synthetic process, and wide-bandgap.[26–28] In a few reported works, the photocatalytic efficiency of ZnO was discovered to be superior to TiO_2 due to its wide bandgap.[29,30]

Zinc oxide (ZnO) nanoparticles are described as a dynamic photocatalyst with integrative properties like wide-bandgap (3.2–3.4 eV), high excitation binding energy (60 meV), high electron mobility, good thermal conductivity, great transparency in the visible range, and produces electron–hole pair under both UV and visible light irradiation[31–33] and ZnO have more photogenerated charge carriers to efficiently produce hydroxyl radical, superoxide, and singlet oxygen respectively, which can reduce and oxidize the organic pollutants completely into their respective final products (CO_2 and H_2O).[34] However, inherent features of ZnO, such as low quantum efficiency, photocorrosion, and incomplete visible light-harvesting, have severely limited its practical applicability in the dye degradation process under the visible-light part of solar light. In order to enhance sunlight harvesting, an effective technique that incorporating a ZnO photocatalyst with other visible light active photocatalyst (g-C_3N_4) has been developed in this work. More significantly, ZnO nanoparticles are used in an increasing number of industrial applications such as paint, rubber, cosmetics, coating, concrete production, electronics, photocatalysis, electrotechnology industries, and biomedicine.[35,36] But ZnO was rarely applied in industries wastewater treatment processes and most researchers barely investigate the reusability efficiency and phytotoxicity evaluation of the treated effluent, emphasizing the novelty of the current study to make sunlight active mesoporous catalyst. Thus, more sunlight will be absorbed on the surface of the composite that improves photocatalytic efficiency.

The primary focus of this study is on the latest innovations in water purification methods based on 2D mesoporous graphitic carbon nitride (g-C_3N_4) nanocomposites beyond 2D nanomaterials. For this purpose, the photocatalytic degradation efficiency of various ratios of ZnO/g-C_3N_4 nanocomposite was tested for synthetic azo dyes such as methylene blue (MB) and rhodamine B (RhB) as a model substrate. This research also looked at the use of this optimized concentration nanocomposite for real textile effluent under sunlight irradiation followed by phytotoxicity assessment on the fenugreek plant (*Trigonella foenum-graecum*). In this regard, the current study aims to look at the health and environmental effects of textile dyes and the potential of non-toxic mesoporous ZnO/g-C_3N_4 nanocomposite that can be used in the purification processes of these dyes pollutants.

2. Experimental procedures

2.1 Materials

All the chemicals used for the fabrication of ZnO/g-C_3N_4 nanocomposites such as zinc nitrate hexahydrate ($Zn(NO_3)_2 \cdot 6H_2O$), sodium hydroxide (NaOH), melamine ($C_3H_6N_6$), ethanol (C_2H_5OH), were analytical grade reagents and were purchased from Sigma-Aldrich and methylene blue ($C_{16}H_{18}ClN_3S$) and Rhodamine B ($C_{28}H_{31}ClN_2O_3$), was purchased from SRL chemicals (Mumbai, India). The chemicals listed above were used without further purification. Throughout the experiment, distilled water was used.

2.2 Synthesis of g-C_3N_4

According to previous reports, g-C_3N_4 nanosheets were synthesized by a facile thermal polycondensation of melamine with some modifications.[37] In a conventional synthesis procedure, 5 g of melamine was placed in a closed silica crucible with a cover and heated at 550 °C for 4 h at a heating rate of 5 °C min^{-1} in a muffle furnace. After allowing cooling naturally, using a mortar and pestle, the yellow precipitate was ground into a fine powder and used without further treatment.

2.3 Synthesis of ZnO

Zinc nitrate and sodium hydroxide were used as precursors in a simple sol–gel technique to make ZnO nanoparticles.[38] The aqueous solution of 0.2 M of $Zn(NO_3)_2 \cdot 6H_2O$ was reduced using 9.5 mL of 2 M NaOH. The reducing agent NaOH was added dropwise to raise the pH 11 under constant stirring, which results in the formation of a white suspension, and stirred for 2 h. The reaction solution was then stirred at room temperature for 2 h. To extract contaminants, the white precipitates were centrifuged and washed with de-ionized water and ethanol. Finally, the samples were dried in an oven at 200 °C for 2 h. During the drying process, the conversion of zinc hydroxide into ZnO took place.

2.4 Synthesis of ZnO/g-C_3N_4 binary nanocomposites

A facile one-step calcination method was used to produce ZnO/g-C_3N_4.[39] To establish the ZnO/g-C_3N_4, synthesized ZnO and melamine were vigorously ground to produce a homogeneous mixture, which was continuously conveyed to a silica crucible to calcinate at 550 °C for 4 h. The synthesized ZnO and melamine

were carefully regulated to achieve ZnO/g-C_3N_4 mole ratios of ZnO: g-C_3N_4 was 0.25 : 1, 0.50 : 1, 0.75 : 1, and 1 : 1.

2.5 Characterization studies

X-ray diffraction analysis was performed on the prepared nanocomposites using a Rigaku Ultima III instrument with Cu-Kα, which has a characteristic wavelength of $\lambda = 1.5406$ Å, and the results were collected over a scanning range of $2\theta = 10^\circ$ to 90°. The UV-vis reflectance of the catalysts was measured using diffuse reflectance spectroscopy (DRS) at room temperature on a Shimadzu, UV 3600 plus in the wavelength range of 200–800 nm. The thermogravimetric analysis (TGA) was performed with a NETZSCH STA 2500 thermogravimetric analyzer in the temperature range of 35–800 °C with a heating rate of 10 °C min^{-1} under nitrogen atmosphere. FE-SEM and elemental mapping through a Scanning electron microscope (SEM) and energy dispersive X-ray analysis (EDX) elemental mapping were studied using FEI Quanta FEG200 (FESEM). The samples were then examined using transmission electron microscopy (Model: TEM, 2100 Electron microscopy). Using a Kratos Axis instrument with mono-energetic Al kα x-rays, the chemical oxidation states of ZnO/g-C_3N_4 nanocomposite were investigated through an X-ray photoelectron spectrometer (XPS). Brunauer–Emmett–Teller (BET) the N_2 adsorption–desorption isotherm in an Autosorb iQ (quantachrome instruments version 5.0) was measured to obtain surface area and textural properties. The pore size distributions were determined using the Barrett–Joyner–Halenda's (BJH) method.

2.6 Photocatalytic degradation of synthetic azo dyes

The photocatalytic activity of g-C_3N_4, ZnO and various ratios of ZnO/g-C_3N_4 nanocomposite were measured on two synthetic azo dye solutions such as methylene blue (MB), and rhodamine B (RhB). The synthesized samples were added at a dose of 20 mg per 50 mL of 15 ppm dye solutions. To assure that equilibrium was attained between the adsorption and desorption of dye molecules on the catalyst surface the solution was continuously stirred in dark conditions for 30 minutes.[40] Afterward, the reaction mixture was exposed to sunlight for 120 min. To determine the intensity of dye solutions with the help of a UV-vis spectrophotometer, every 30 min a 3 mL of the dye sample was collected.[41–43] The following formula was used to calculate the percentage (%) of dye degraded when exposed to sunlight. The non-catalyst- treated control was used to subtract the degradation measured in catalyst-treated controls.[44]

$$\text{Dye degradation (\%)} = (C_o - C_t)/C_o \times 100,$$

where (C_o) denoted the starting dye concentration and (C_t) denoted the final dye concentration.

2.7 Real textile effluent treatment

The real textile effluent was collected from drains of various dye industries located in Ayyampettai (Kancheepuram, Tamilnadu, India).[45] The textile wastewater samples have been collected in plastic bottles and immediately transported to the lab for treatment. Initially, 100 mL of textile effluent was irradiated with sunlight in the absence of the catalyst. The textile effluent had no decoloration at first, as per our preliminary results. It was hence concluded that the textile effluent did not undergo any self-degradation.[46] The efficiency of g-C_3N_4, ZnO, and various ratios of ZnO/g-C_3N_4 for textile wastewater treatment was then studied as a batch experiment in a 200 mL beaker containing 100 mL wastewater. The experiment was conducted separately for each catalyst without dilution of textile effluent. Each nanocatalyst was weighed at 75 mg and mixed with a 100 mL wastewater sample. The reaction mixtures were stirred for 30 min under the dark condition to establish the adsorption–desorption equilibrium condition. Suspensions were then exposed to sunlight for 120 min with vigorous stirring. According to Fouda *et al.*, physico-chemical parameters (such as pH, EC, temperature, BOD, COD, and TDS) were investigated in both treated and non-treated samples.[47] Furthermore, the titrimetric procedures were used to determine chlorides, sulphates, and hardness of treated and non-treated textile effluent samples.[48,49]

2.8 Phytotoxicity analysis of textile effluent

To investigate the toxic effects of textile effluents and their degraded products after photocatalytic degradation; the phytotoxicity study was performed on common agricultural crop fenugreek (*Trigonella foenum-graecum*). The seeds were planted in 10 kg of paddy field soil in pots.[50] 20 fenugreek (*Trigonella foenum-graecum*) seeds were treated separately with 10 mL of textile solutions and degraded textile dye solution per 24 hours. As a control, seeds were planted in pots were treated with distilled water.[51] For 15 days, all pots were kept in the shade near sunlight. Germination of seeds treated with textile effluent and degraded effluent solutions were calculated after comparing with control. At the end of the germination experiment, the plant height, fresh weight, dry weight, and germination percentage of seedlings were measured separately for textile effluent, degraded textile effluent, and control samples.[52]

3. Results and discussion

3.1 X-ray diffraction analysis

XRD analysis is a useful method to evaluate the nanoparticles, crystalline structures, phase identification, purity, and crystallite diameter of the prepared nanomaterials. The powder XRD patterns of the prepared g-C_3N_4, ZnO, and 0.75 : 1 ZnO/g-C_3N_4 nanocomposite are shown in Fig. 1. The pure g-C_3N_4 nanosheets have two different peaks at $2\theta = 13.34^\circ$ and 27.38° which belong to (100) and (002) diffraction planes (JCPDS no. 87-1526). The XRD pattern of ZnO nanoparticles monitor peaks at 31.8°, 34.43°, 36.27°, 47.57°, 56.67°, 62.9°,67.99°, and 69.20° with corresponding diffraction planes (100), (002), (101), (102), (110), (103), (112), and (201) respectively. The XRD peaks indicate that the ZnO nanoparticles correspond to the hexagonal wurtzite structure (JCPDS card no. 89-0510).[53] The sharp and intense diffraction peaks of both g-C_3N_4 and ZnO demonstrated their crystalline existence in this regard. The XRD patterns of the

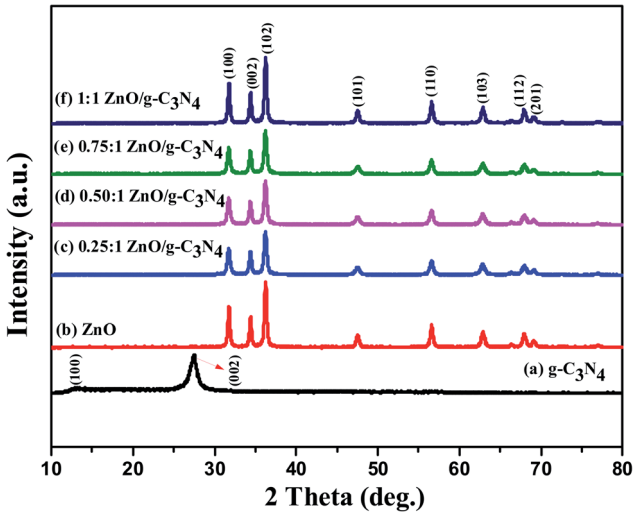

Fig. 1 X-ray diffraction patterns of g-C_3N_4, ZnO, and ZnO/g-C_3N_4 nanocomposites.

synthesized ZnO/g-C_3N_4 nanocomposites have the same distinct diffraction peaks as bare-ZnO. ZnO crystalline peaks existed at the ZnO/g-C_3N_4 composites after the incorporation of ZnO over the g-C_3N_4. The characteristic peak of g-C_3N_4 is not observed in the XRD pattern of 0.75 : 1 ZnO/g-C_3N_4 composite, which is possibly due to the broken hydrogen bond interrupts the interlayer periodic stacking, lowering the length of inner layer tri-*s*-triazine repeating units, and expanding layer spacing by a self-assembly process.[54,55]

3.2 Optical properties and band gap

UV-visible diffuse reflectance spectroscopy was used to determine the optical properties of the photocatalysts as-prepared (Fig. 2a) and band gap energy values of the prepared nanocomposites were estimated by plotting the Kubelka–Munk function,[56] as shown in Fig. 2b. The reflectance band edge of the ZnO sample occurs at 370 nm, corresponding to a band gap of 3.23 eV and g-C_3N_4 has a fundamental absorption edge at 398 nm, corresponding to a band gap of 2.76 eV. After the addition of ZnO to the g-C_3N_4, the band edge of 0.25 : 1 ZnO/g-C_3N_4, 0.50 : 1 ZnO/g-C_3N_4, 0.75 : 1 ZnO/g-C_3N_4, 1 : 1 ZnO/g-C_3N_4 photocatalysts was slightly extended to the visible light region, and showed an evident red shift gradually with an increasing loading amount of ZnO, suggesting that the band gaps of these composites are reduced and those band gap values are provided in Table 1. Those composites exhibit a strong visible-light absorption, which leads to the generation of more photo-generated electrons and holes and thus leads to enhanced photocatalytic activity.

3.3 Thermal analysis (TGA)

To understand the thermal stability of the synthesized samples such as g-C_3N_4, ZnO, and various ratios of ZnO/g-C_3N_4 nanocomposites, as well as weight loss of the composites, were analyzed using TGA analysis. Thermogravimetric analysis was carried out at a heating rate of 20 °C min^{-1} from room temperature to 800 °C. When the temperature is above 550 °C, the g-C_3N_4 nanosheets are unstable, as shown in Fig. 3a, and the weight loss of g-C_3N_4 started at this temperature.[57] As the temperature exceeds 750 °C, almost all of the g-C_3N_4 nanosheets burn into gases and the remaining mass is nearly zero. Fig. 3b shows the TGA curve of ZnO nanoparticles, in which a very small weight loss (~2 wt%) is occurred below 300 °C, probably due to the removal of physically and chemically adsorbed water on their surface. The weight of the ZnO/g-C_3N_4

Table 1 Optical band gap value for photocatalysts

Catalyst	Optical band gap energy (eV)
g-C_3N_4	2.70
ZnO	3.20
0.25 : 1 ZnO/g-C_3N_4	2.72
0.50 : 1 ZnO/g-C_3N_4	2.69
0.75 : 1 ZnO/g-C_3N_4	2.60
1 : 1 ZnO/g-C_3N_4	2.62

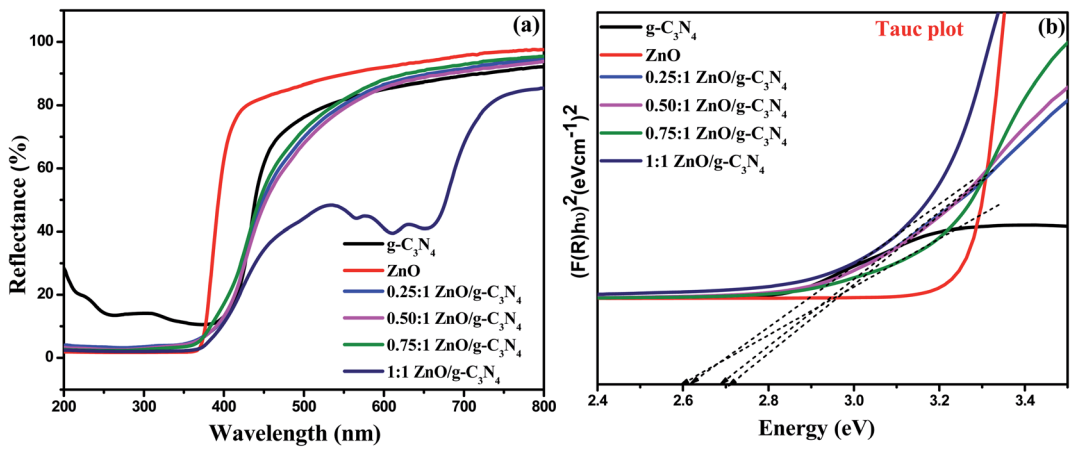

Fig. 2 (a) UV-vis DRS spectra and (b) Tauc plot for the evaluation of band gap values of g-C_3N_4, ZnO, and ZnO/g-C_3N_4 nanocomposites.

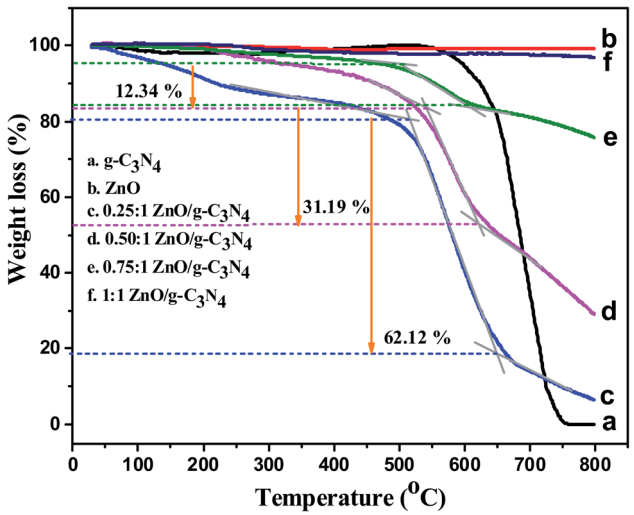

Fig. 3 The TGA curves of (a) g-C_3N_4, (b) ZnO, (c) 0.25 : 1 ZnO/g-C_3N_4, (d) 0.50 : 1 ZnO/g-C_3N_4, (e) 0.75 : 1 ZnO/g-C_3N_4, (f) 1 : 1 ZnO/g-C_3N_4 nanocomposites.

nanocomposites decreased rapidly in the temperature range 500–650 °C, as shown in Fig. 3c–e, suggesting that g-C_3N_4 combustion occurred in this temperature range. Accordingly the total weight loss of 0.25 : 1 ZnO/g-C_3N_4, 0.50 : 1 ZnO/g-C_3N_4, and 0.75 : 1 ZnO/g-C_3N_4, is about 62.12%, 31.19%, and 12.34%. Fig. 3f displays the TGA curve of the 1 : 1 ZnO/g-C_3N_4 composite. The residual weight of this composite is about 97.5 wt%. This less weight loss of the nanocomposite is due to the increasing amount of ZnO ratio in the composite. It confirms that the thermal stability of the nanocomposite increases after the incorporation of ZnO into the g-C_3N_4 nanosheets.

3.4 Material morphological analysis (FE-SEM-EDS and TEM)

The surface morphology of the g-C_3N_4, ZnO, and 0.75 : 1 ZnO/g-C_3N_4 nanocomposite were investigated through FE-SEM as presented in Fig. 4. As shown in Fig. 4a FE-SEM images of g-C_3N_4 are comprised of nanosheet-like structures and fluffier. ZnO nanoparticles fabricated by Sol–gel have an irregularly aggregated spherical particle (Fig. 4b). However, the surface morphology of fabricated 0.75 : 1 ZnO/g-C_3N_4 nanocomposite (Fig. 4c and d) containing both ZnO and g-C_3N_4 has a nanosheets appearance with shrunken edges and irregular morphology and were homogeneously dispersed without porous structure. This surface morphology might be due to the increase in calcination temperature of ZnO after combination with g-C_3N_4 and it confirms that zinc and oxygen elements were distributed between carbon and nitrogen, indicating that ZnO was successfully combined onto the surface of g-C_3N_4 nanosheets and the prepared composite is mesoporous in nature. As a result, the materials used to fabricate binary nanocomposites are expected to play a crucial role in determining their photocatalytic efficiency. The SEM-mapping images shown in Fig. 5 proved the existence of all constituent elements (*i.e.*, C, N, Zn, and O) in the ZnO/g-C3N4 structure. Furthermore, as shown in Fig. 5, the concentrations of the elements present in the ZnO/g-C_3N_4 nanocomposite indicate that Zn and O elements have

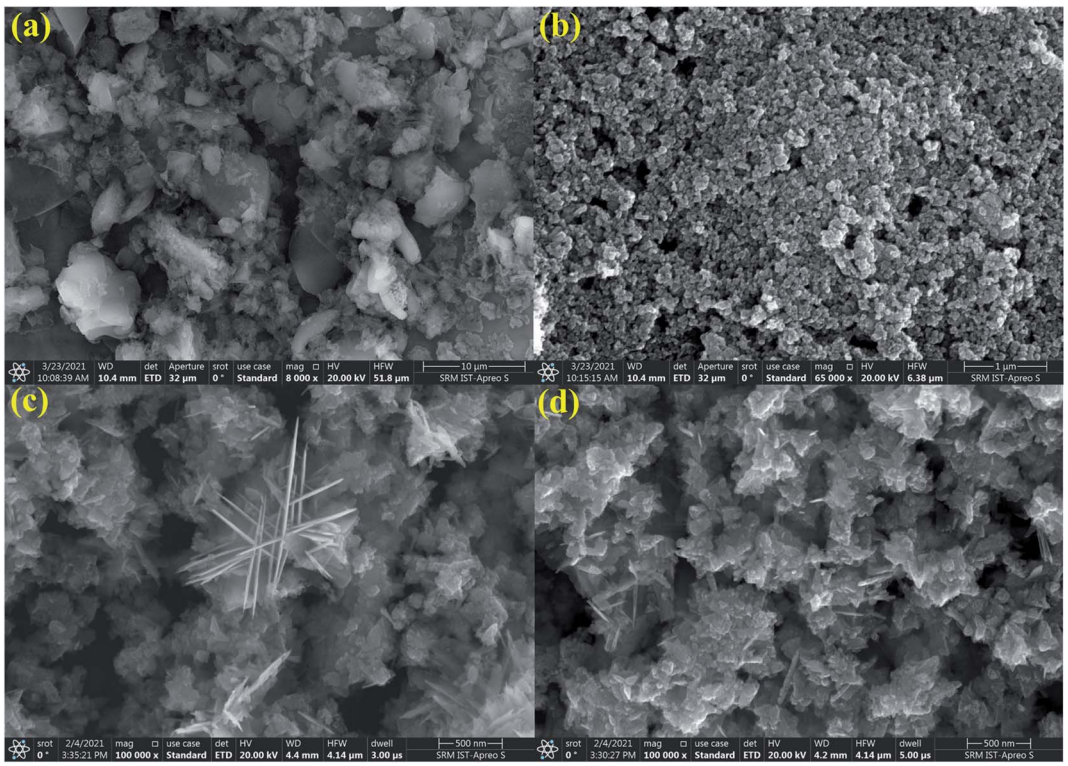

Fig. 4 FE-SEM images of (a) g-C_3N_4, (b) ZnO, (c) and (d) 0.75 : 1 ZnO/g-C_3N_4 nanocomposite.

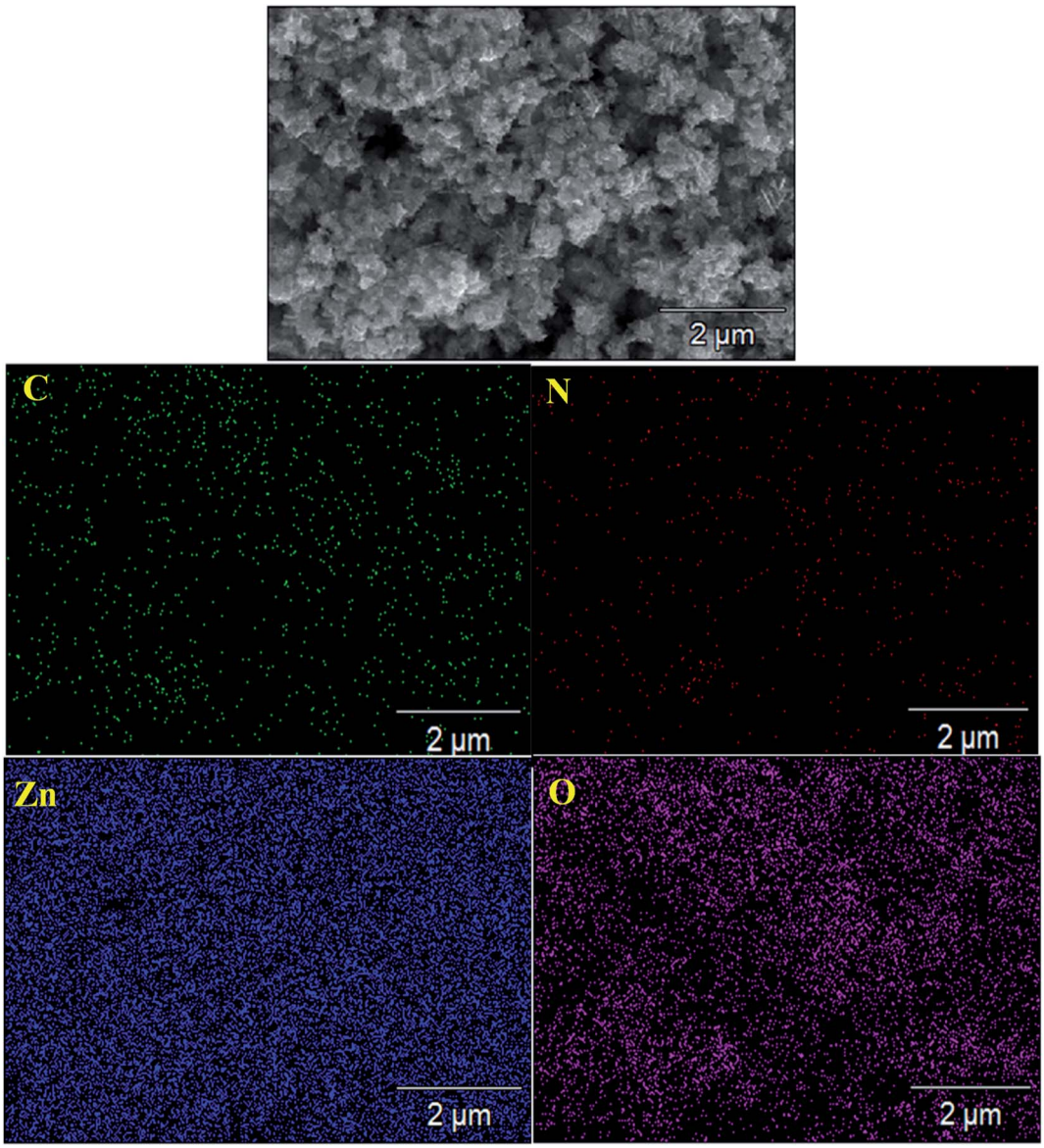

Fig. 5 SEM elemental mapping image of 0.75 : 1 ZnO/g-C_3N_4 nanocomposite.

higher concentrations than C and N. This is due to the complete deposition of Zn and O elements on the surface of g-C_3N_4. This result is evidence for the ZnO modified g-C_3N_4 heterostructure photocatalyst system.

Further topography of the 0.75 : 1 ZnO/g-C_3N_4 nanocomposite is carried out by Transmission electron microscopy (TEM) analysis as illustrated in Fig. 6. As shown in Fig. 6(a–c) it can be observed that TEM images with 50 nm, 20 nm, and 10 nm scales depict darker ZnO nanoparticles were dispersed irregularly on the g-C_3N_4 sheets and g-C_3N_4 nanosheets have small thin flat irregular two-dimensional layer shape, which is compatible with the FE-SEM images. The TEM image also reveals a mesoporous structure in the photocatalyst sample, as well as an aggregation of nanosheets. From Fig. 6c it can be observed that an obvious smooth interface is produced between ZnO and g-C_3N_4. The interface between g-C_3N_4 nanosheets and ZnO particles is beneficial to improving photocatalytic degradation activity by providing more surface active sites and a small diffusion length for lowering recombination probability and thus improving the separation of photo-excited charge carriers, according to these morphological investigations.

3.5 X-ray photoenergy spectroscopy (XPS)

The oxidation state and surface chemical composition of the prepared 0.75 : 1 ZnO/g-C_3N_4 nanocomposite were investigated using the X-ray photoelectron spectrum (XPS). Fig. 7a provides the wide range of XPS spectra of the composite sample that clearly show the presence of Zn, O, N, and C elements. The deconvoluted peaks at 284.6, 286.3, and 288.2 eV in the high-resolution C 1s range in Fig. 7b are attributed to carbon-containing contamination, sp^2 hybridized carbon in the g-C_3N_4 lattice, adventitious carbon C–C, residual C=O, and

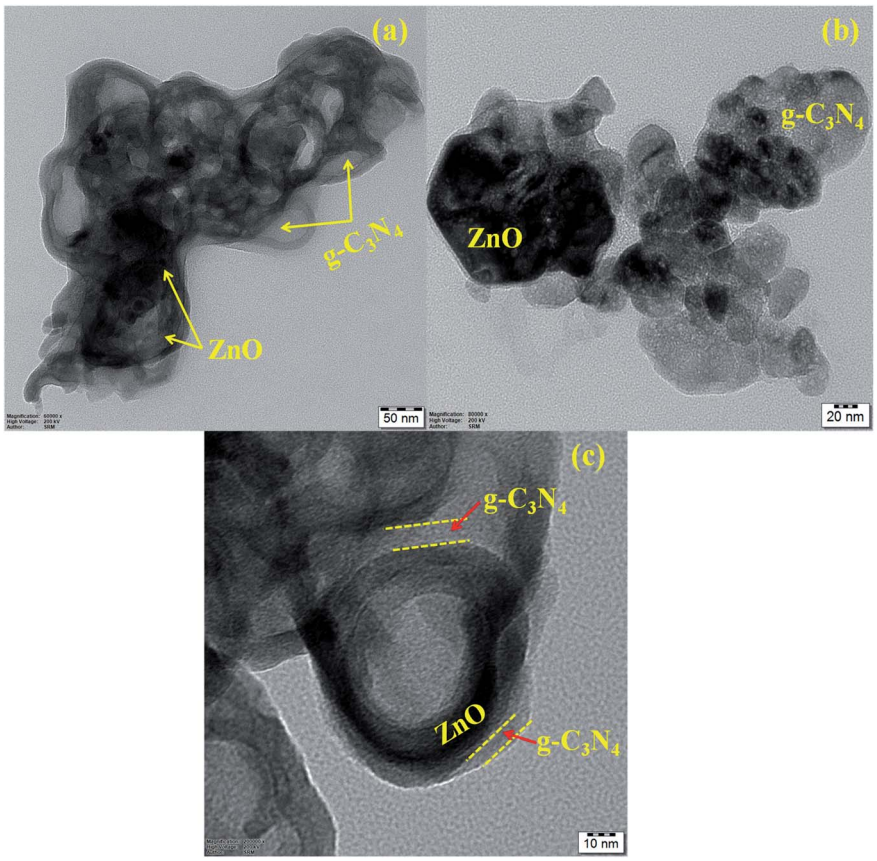

Fig. 6 TEM images of 0.75 : 1 ZnO/g-C_3N_4 nanocomposite with various scale (a) 50 nm, (b) 20 nm, & 10 nm.

aromatic structure (N–C=N), respectively.[58] The N1s spectrum contains four types of binding energies 398.6, 399.5, 401.1 eV, and 404.2 eV displayed for O–Zn–N, C–N=C, N–H, and N=N functional groups respectively as shown in Fig. 7c, and these findings are in good agreement with the literature.[59] The binding energies of Zn 2p3/2 and Zn 2p1/2, as shown in Fig. 7d, are 1021.7 and 1044.6 eV, respectively, and are due to Zn in the bivalent state. The formation of N–Zn bonds causes a chemical shift in the ZnO/g-C_3N_4 nanocomposite, as shown in Fig. 7d. XPS analysis suggests that chemical bonds occur between the two semiconductors in the formation of the 0.75 : 1 ZnO/g-C_3N_4 nanocomposite. This type of interaction assists in the creation of heterojunctions and, as a result, improves charge transfer and separation. Also, at the O 1s XPS spectrum shown in Fig. 7e corresponding to binding energies at 530.2 eV can be related to the O^{2-} ions in ZnO, whereas the wider peak at 531.4 eV can be associated to the OH^-, H_2O, O_2 group absorbed onto the photocatalyst's surface.[60]

3.6 BET analysis

For the comparison of the photocatalytic activity of prepared catalysts, the surface area, pore volumes, and pore size were determined by nitrogen adsorption and desorption isotherms. Fig. 8a and b shows the isotherms of nitrogen adsorption and desorption and pore size distribution curve of g-C_3N_4 and 0.75 : 1 ZnO/g-C_3N_4. The g-C_3N_4 sample exhibits type IV with H_3 hysteresis loops, while the 0.75 : 1 ZnO/g-C_3N_4 nanocomposite exhibits type IV with H_4 hysteresis loops, as shown in Fig. 8a. However, both samples revealed the existence of mesopores. According to the BET method, the S_{BET} of g-C_3N_4 and 0.75 : 1 ZnO/g-C_3N_4 was 8.47 $m^2\ g^{-1}$ and 19.54 $m^2\ g^{-1}$ respectively. The surface area of the 0.75 : 1 ZnO/g-C_3N_4 composite is higher than g-C_3N_4. To improve the photocatalytic activity, the large surface area of the sample is beneficial for the absorption of light, organic dye adsorption, and offers a more active site for the photocatalytic process.[61] In comparison to a g-C_3N_4 nanosheets pore size of 8.6 nm, the pore size distribution of 0.75 : 1 ZnO/g-C_3N_4 composite seems to be in the 15.2 nm range and exists as large-sized mesopores (Fig. 8b). As a result, the surface of the composite sample will absorb more sunlight, which improves photocatalytic efficiency.

4. Applications in water treatment

4.1 Photocatalytic degradation activity using synthetic dyes

A few model cationic dyes, such as methylene blue (MB) and rhodamine B (RhB), were used in the dye degradation experiments. Photoinduced self-degradation of MB and RhB is conducted without catalyst under the same experimental condition. The degradation efficiency of the MB and RhB dyes when self-pyrolyzed is just 5%, while the degradation efficiency of the separate g-C_3N_4 and ZnO nanoparticles for MB dye is 56% and

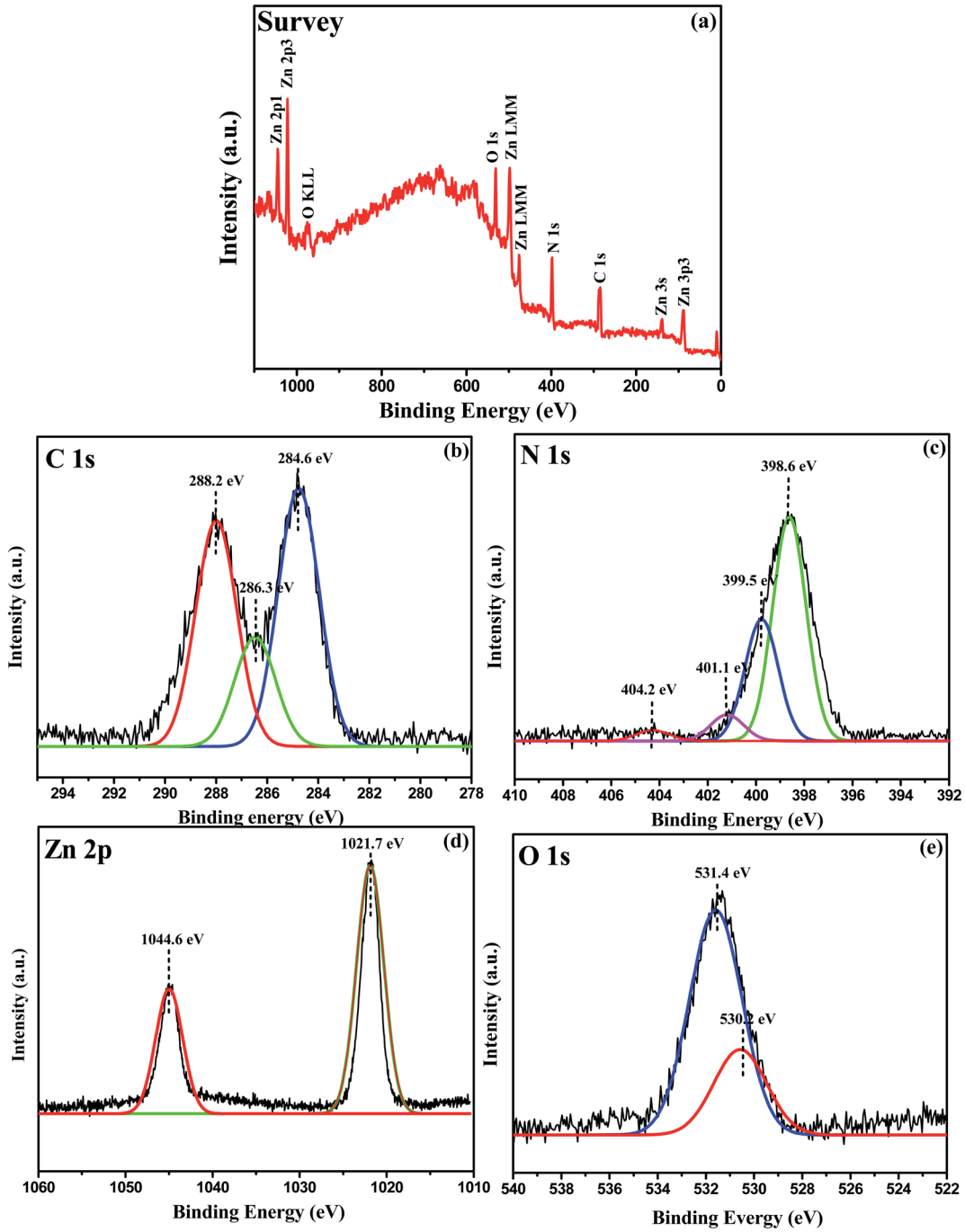

Fig. 7 XPS spectra of 0.75 : 1 ZnO/g-C_3N_4 (a) Full scan XPS survey spectra of the nanocomposite containing C, N, O, and Zn elements, (b) C 1s, (c) N 1s, (d) Zn 2p, and (e) O 1s.

38% and RhB dye degraded up to 46% and 30% respectively. In brief, to optimize the best photocatalytic activity of various ratios of ZnO/g-C_3N_4 nanocomposite the aqueous solutions of both dyes were prepared at a concentration of 15 ppm, and 20 mg of g-C_3N_4, ZnO, and ZnO/g-C_3N_4 catalyst were added to 50 mL of each dye solution separately. To establish the adsorption–desorption equilibrium of the dye on the surface of the photocatalyst, dark experiments were conducted out by holding the suspensions in the dark for 30 min, after that 3 mL of solution is drawn to monitor the adsorption process, UV-vis absorption spectra were recorded. The suspensions were then exposed to sunlight for 2 h on a bright sunny day. After the sunlight exposure, 0.25 : 1 ZnO/g-C_3N_4, 0.50 : 1 ZnO/g-C_3N_4, 0.75 : 1 ZnO/g-C_3N_4, 1 : 1 ZnO/g-C_3N_4 binary nanocomposites shows photocatalytic degradation efficiency of 80.85%, 89.32%, 98.6% and 93.48% against MB dye and 78.5%, 87.7%, 94.5% and 91.82% against RhB dye respectively and it is shown in Fig. 9. Due to the development of an efficient heterojunction

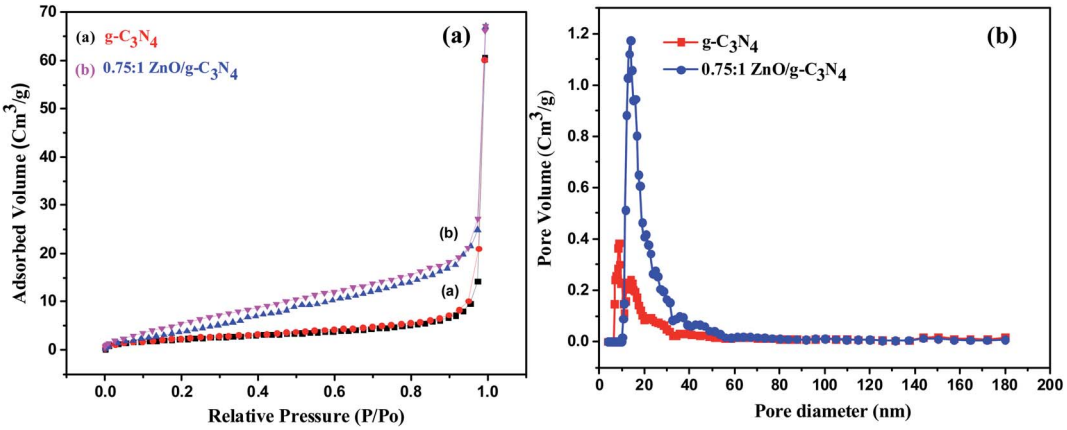

Fig. 8 (a) Nitrogen adsorption–desorption isotherms and (b) pore size distribution curves of g-C_3N_4 and 0.50 : 1 ZnO/g-C_3N_4.

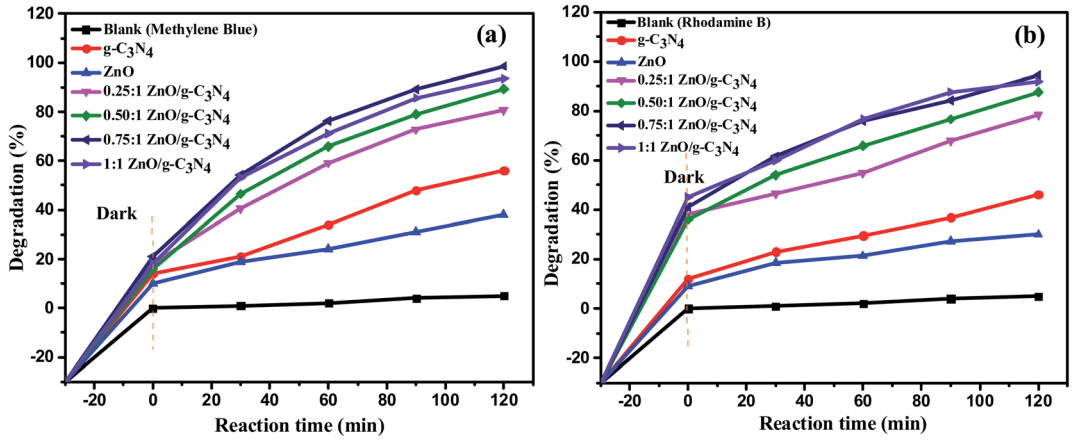

Fig. 9 The variation of photocatalytic degradation rate (%) of (a) MB (b) RhB dye over various catalysts and time of irradiation (min).

between the g-C_3N_4 and ZnO, the 0.75 : 1 ZnO/g-C_3N_4 binary nanocomposite has relatively improved dye degradation efficiency among the nanocomposites. Further, 0.75 : 1 ZnO/g-C_3N_4 binary nanocomposite is used for the treatment of textile effluent, phytotoxicity, and recycling process under sunlight irradiation. UV-vis absorbance spectra have been used to monitor the reaction progress. Fig. 10 displays the UV-vis absorption spectra of MB and RhB degradation using 0.75 : 1 ZnO/g-C_3N_4 nanocomposite in the presence of sunlight. The plausible mechanism for sunlight assisted photocatalytic degradation of MB and RhB in the presence of 0.75 : 1 ZnO/g-C_3N_4 nanocomposite is given as ESI†.[62,63]

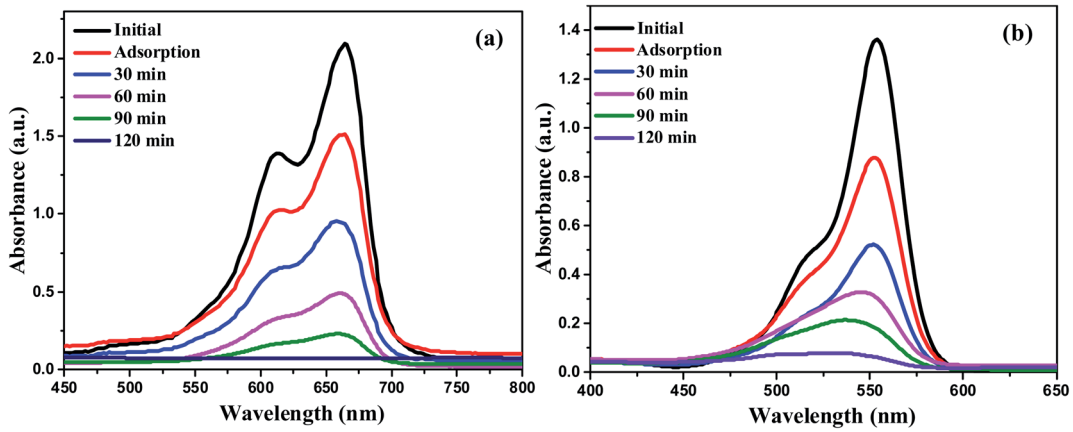

Fig. 10 UV-vis absorption spectra of (a) MB and (b) RhB dye degradation using 0.75 : 1 ZnO/g-C_3N_4 nanocomposite.

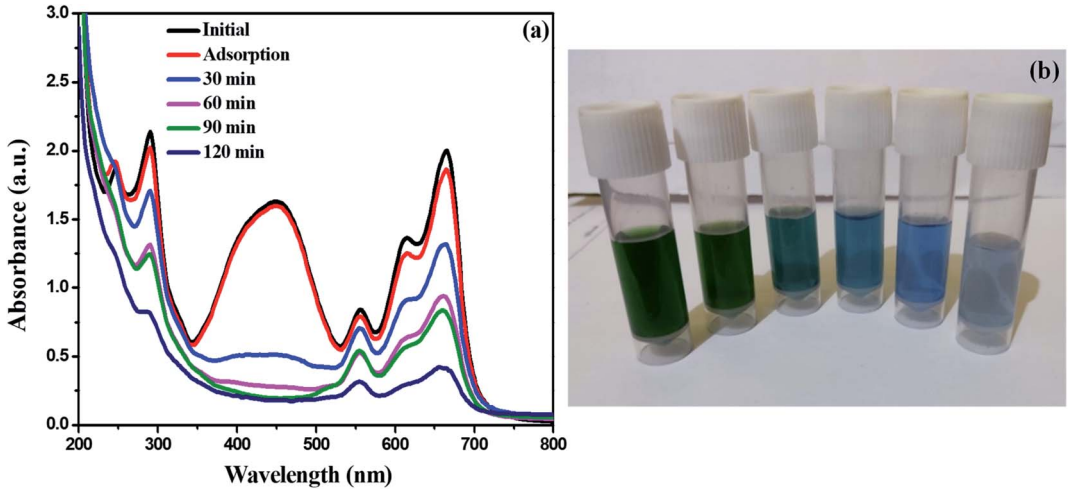

Fig. 11 (a) UV-vis absorption spectra of textile effluent degradation using 0.75 : 1 ZnO/g-C_3N_4 nanocomposite (b) decrease in color intensity of textile effluent.

4.2 Photocatalytic degradation of real textile wastewater

Industrial dyes have a wide range of chemical constituents that are selected depending on the type of materials to be dyed. As a consequence, dyeing effluent has a different colour and chemical composition. However, there is a considerable amount of reduction in color of textile effluent (degradation rate-80%) was noticed after photocatalytic degradation using synthesized 0.75 : 1 ZnO/g-C_3N_4 catalyst within 120 min of observation. Fig. 11 displays the UV-vis absorption spectra of textile effluent degradation using 0.75 : 1 ZnO/g-C_3N_4 nanocomposite in the presence of sunlight. Furthermore, when comparing non-treated effluent samples to those treated with 0.75 : 1 ZnO/g-C_3N_4 catalyst at 75 mg concentration, all physico-chemical parameters such as pH, EC, temperature, BOD, COD, TDS, Chloride, Sulphate, and Hardness showed a substantial decrease in concentration, and the values were given in Table 2.

4.3 Phytotoxicity analysis

Dyeing effluents discharged into water streams without treatment can cause a serious threat to the environment as well as health risks to humans.[64] Considering that we determined the phytotoxicity of the real textile effluent before and after photocatalytic degradation and treated dye-containing wastewater can be reused in agriculture. The phytotoxicity of actual textile effluent and its derivatives after photocatalytic degradation is examined for fenugreek plant germination (*Trigonella foenum-graecum*) and after 15 days the germinated plant is shown in Fig. 12 and Table 3 shows growth parameters for fenugreek plants, including germination percentage, plant length, fresh weight, and dry weight. The results of the phytotoxicity experiment observed that compared to the seeds germinated in distilled water, untreated dye-containing wastewater was reducing the germination percentage of fenugreek plants, while they grew better in treated dye-containing wastewater, suggesting that the toxicity of the dye-containing solution was reduced after being treated by the 0.75 : 1 ZnO/g-C_3N_4 catalyst. The results suggest that using 0.75 : 1 ZnO/g-C_3N_4 nanocomposite in photocatalytic degradation of textile effluent is secure, which in turn is suggesting that it may be used in real applications.

Table 2 Physico-chemical parameter analysis of textile wastewater before and after treatment by the optimal concentration (75 mg of nanocomposite/100 mL textile effluent)

Various parameters	Non-treated	Treated
pH	8.27	6.78
EC (dS m^{-1})	5.24	2.60
Temperature (°C)	32	32
BOD (mg L^{-1})	328.29	245.38
COD (mg L^{-1})	1034.06	578.67
TDS (mg L^{-1})	1478.80	785.10
Sulphate (mg L^{-1})	526	352.25
Chloride (mg L^{-1})	498.34	256.65
Hardness (mg L^{-1})	678.60	278.34

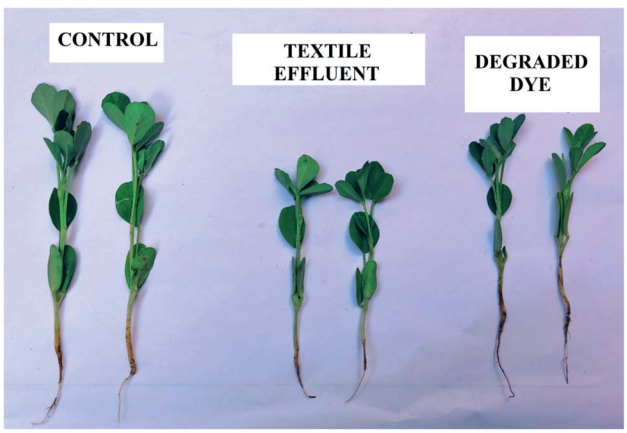

Fig. 12 Phytotoxicity analysis after 15 days of fenugreek plant growth using distilled water, textile effluent, and degraded dye effluent solution.

Table 3 Phytotoxicity evaluation of non-treated and treated textile effluent using fenugreek seeds

Parameters	Control	Non-treated	Treated
Germination (%)	100	70.03	88.45
Plant height (cm)	15.6	9.6	13.2
Plant fresh weight (g)	0.9876	0.6906	0.8734
Plant dry weight (g)	0.1984	0.0689	0.1052

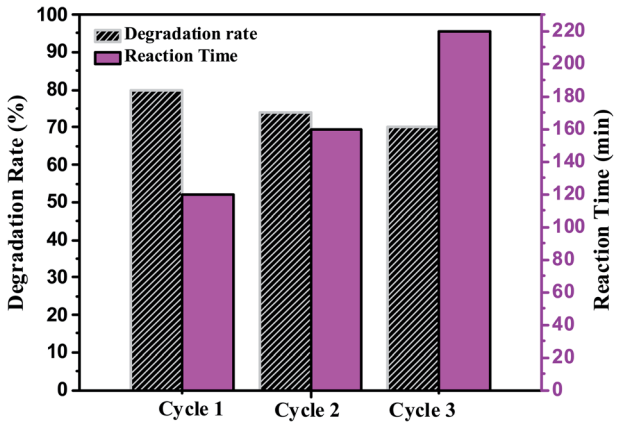

Fig. 13 Determination of the reusability of synthesized 0.75 : 1 ZnO/g-C_3N_4 catalyst for the photocatalytic degradation of textile effluent.

4.4 Reusability and stability of the 0.75 : 1 ZnO/g-C_3N_4 catalyst during the photocatalytic degradation of textile effluent

Photocatalytic stability and reusability of the synthesized nanocomposite were studied by repeating the photocatalytic degradation process two times at optimum conditions (75 mg catalyst and 100 mL of textile effluent). Fig. 13 shows the plot of degradation rate (%) and reaction time (min) V_s the number of the cycle using 0.75 : 1 ZnO/g-C_3N_4 nanocomposite. After each cycle, the catalyst can be easily separated using the precipitation and centrifugation method and reused with a newly taken textile effluent. The foregoing results point out that 0.75 : 1 ZnO/g-C_3N_4 catalyst was found effective and reusable under sunlight. Fig. 13 shows that after the completion of three cycles the catalyst efficiency decreased up to 10%. There has been no significant decrease in photocatalytic activity up to three cycles. For the first cycle, the degradation rate is 80% and for the second and third cycles, the degradation efficiency is 74.28% and 70.34%. However, after the first cycle, a longer incubation period was needed for better degradation of textile effluent.[65] These findings also support the feasibility of using this technology in real-world wastewater treatment.

5. Conclusion

The various ratios of ZnO/g-C_3N_4 (0.25 : 1, 0.50 : 1, 0.75 : 1, and 1 : 1) binary nanocomposites were successfully synthesized *via* the simple one-step calcination method. The photocatalytic activities of synthesized catalysts were investigated by photocatalytic degradation of MB and RhB dye under sunlight for 120 min. The optimized mesoporous 0.75 : 1 ZnO/g-C_3N_4 nanocomposite showed high photocatalytic degradation efficiency of 98.6% and 94.5% against MB and RhB dye which is two times higher than that of g-C_3N_4 (2.19%) as well as long term stability than other catalysts. The main reason could be suggested that the photocatalytic enhancement of the mesoporous nanocomposites is mainly attributed to the combined effect between g-C_3N_4 and ZnO which results in efficient charge separation, enhanced sunlight absorption, and increased amount of the surface hydroxyl group. The toxicity of the degraded textile effluent after photocatalytic treatment was reduced and the value of different physico-chemical parameters of textile effluents was decreased after treatment. The developed photocatalytic process using 0.75 : 1 ZnO/g-C_3N_4 exhibited excellent efficiency and it could be applied in the treatment of existing textile effluents due to the advantages of its more facile, non-toxic, low cost and stable, recyclability, and remarkable output.

Author contributions

H. Leelavathi: methodology, software, writing – original draft, visualization, investigation, N. Abirami and Helen P. Kavitha: formal analysis, R. Muralidharan: writing – review & editing, S. Tamilarasan and S. Sangeetha: data curation, R. Arulmozhi: writing – review & editing, supervision.

Conflicts of interest

The authors declare no competing financial interest.

Acknowledgements

The authors wish to acknowledge DST-FIST (fund for the improvement of S&T) for the financial assistance at the Department of Chemistry, SRM Institute of Science and Technology (grant no SR/FST/CST-266/2015(c))

References

1 N. Mohammed, N. Grishkewich and K. C. Tam, *Environ. Sci.: Nano*, 2018, **5**, 623–658.
2 A. Ahmad, S. H. Mohd-Setapar, C. S. Chuong, A. Khatoon, W. A. Wani, R. Kumar and M. Rafatullah, *RSC Adv.*, 2015, **5**, 30801–30818.
3 C. Liu, C. Wang, Y. Guo, J. Zhang, Y. Cao, H. Liu, Z. Hu and C. Zhang, *J. Mater. Chem. A*, 2019, **4**, 1–29.
4 A. A. Yaqoob, N. Habibah, A. Serr, M. Nasir and M. Ibrahim, *Nanomaterials*, 2020, **10**, 932–956.
5 M. J. López-Serrano, J. F. Velasco-Muñoz, J. A. Aznar-Sánchez and I. M. Román-Sánchez, *Sustain.*, 2020, **12**, 1–20.
6 R. Saravanan, V. K. Gupta, V. Narayanan and A. Stephen, *J. Taiwan Inst. Chem. Eng.*, 2014, **45**, 1910–1917.
7 A. B. Holmes and F. X. Gu, *Environ. Sci.: Nano*, 2016, **3**, 982–996.

8 C. Gadipelly, A. Pérez-González, G. D. Yadav, I. Ortiz, R. Ibáñez, V. K. Rathod and K. V. Marathe, *Ind. Eng. Chem. Res.*, 2014, **53**, 11571–11592.
9 P. Kehrein, M. Van Loosdrecht, P. Osseweijer, M. Garfí, J. Dewulf and J. Posada, *Environ. Sci.: Water Res. Technol.*, 2020, **6**, 877–910.
10 A. Fouda, S. E. D. Hassan, E. Saied and M. S. Azab, *J. Environ. Chem. Eng.*, 2021, **9**, 104693.
11 K. Singh and S. Arora, *Crit. Rev. Environ. Sci. Technol.*, 2011, **41**, 807–878.
12 M. Ahmaruzzaman and V. K. Gupta, *Ind. Eng. Chem. Res.*, 2011, **50**, 13589–13613.
13 M. Ismail, K. Akhtar, M. I. Khan, T. Kamal, M. A. Khan, A. M. Asiri, J. Seo and S. B. Khan, *Curr. Pharm. Des.*, 2019, **25**, 3645–3663.
14 I. Ali, C. Peng, I. Naz, D. Lin, D. P. Saroj and M. Ali, *RSC Adv.*, 2019, **9**, 3625–3646.
15 V. K. Gupta, I. Ali, T. A. Saleh, A. Nayak and S. Agarwal, *RSC Adv.*, 2012, **2**, 6380–6388.
16 T. Wei, L. Wu, F. Yu, Y. Lv, L. Chen, Y. Shi and B. Dai, *RSC Adv.*, 2018, **8**, 39334–39340.
17 W. Wang and Z. Shao, *Chem. Soc. Rev.*, 2012, **1–3**, 1–38.
18 A. Bhattacharjee and M. Ahmaruzzaman, *RSC Adv.*, 2013, **1**, 1–38.
19 P. Khare, A. Singh, S. Verma, A. Bhati, A. K. Sonker, K. M. Tripathi and S. K. Sonkar, *ACS Sustainable Chem. Eng.*, 2018, **6**, 579–589.
20 M. Ge, N. Zhu, Y. Zhao, J. Li and L. Liu, *Ind. Eng. Chem. Res.*, 2012, **51**, 5167–5173.
21 A. Bhati, S. R. Anand, D. Saini, Gunture and S. K. Sonkar, *npj Clean Water*, 2019, **2**, 1–9.
22 X. Li, J. Xiong, X. Gao, J. Huang, Z. Feng, Z. Chen and Y. Zhu, *J. Alloys Compd.*, 2019, **802**, 196–209.
23 X. Zhao, D. Pan, X. Chen, R. Li, T. Jiang, W. Wang, G. Li and D. Y. C. Leung, *Appl. Surf. Sci.*, 2019, **467–468**, 658–665.
24 M. Ismael, Y. Wu, D. H. Taffa, P. Bottke and M. Wark, *New J. Chem.*, 2019, **43**, 6909–6920.
25 R. Mohammadi, H. Alamgholiloo, B. Gholipour, S. Rostamnia, S. Khaksar, M. Farajzadeh and M. Shokouhimehr, *J. Photochem. Photobiol., A*, 2020, **402**, 112786.
26 J. Jiang, X. Zhang, P. Sun and L. Zhang, *J. Phys. Chem. C*, 2011, **115**, 20555–20564.
27 H. Park, H. Il Kim, G. H. Moon and W. Choi, *Energy Environ. Sci.*, 2016, **9**, 411–433.
28 M. Pirhashemi, A. Habibi-yangjeh and S. Rahim, *J. Ind. Eng. Chem.*, 2018, **62**, 1–25.
29 S. O. Fatin, H. N. Lim, W. T. Tan and N. M. Huang, *Int. J. Electrochem. Sci.*, 2012, **7**, 9074–9084.
30 Y. Li, W. Xie, X. Hu, G. Shen, X. Zhou, Y. Xiang, X. Zhao and P. Fang, *Langmuir*, 2010, **26**, 591–597.
31 T. Khalafi, F. Buazar and K. Ghanemi, *Nature*, 2019, **9**, 6866–6875.
32 L. Zhou, Z. Han, G. D. Li and Z. Zhao, *J. Phys. Chem. Solids*, 2021, **148**, 109719–109726.
33 T. Ahmed and T. Edvinsson, *J. Phys. Chem. A*, 2020, **6**, 1–33.
34 X. Chen, Z. Wu, D. Liu and Z. Gao, *Nanoscale Res. Lett.*, 2017, **12**, 143–152.
35 R. P. Anupama, M. Anagha, K. O. Shamsheera and J. Abraham, *New J. Chem.*, 2012, **1–3**, 1–13.
36 M. Faizan, A. Faraz, A. R. Mir and S. Hayat, *J. Plant Growth Regul.*, 2021, **40**, 101–115.
37 R. Guan, J. Li, J. Zhang, Z. Zhao, D. Wang, H. Zhai and D. Sun, *ACS Omega*, 2019, **4**, 20742–20747.
38 H. S. Hassan, M. F. Elkady, E. M. El-Sayed, A. M. Hamed, A. M. Hussein and I. M. Mahmoud, *Int. J. Nanoelectron. Mater.*, 2018, **11**, 179–194.
39 N. T. T. Truc, D. S. Duc, D. Van Thuan, T. Al Tahtamouni, T. D. Pham, N. T. Hanh, D. T. Tran, M. V. Nguyen, N. M. Dang, N. T. P. Le Chi and V. N. Nguyen, *Appl. Surf. Sci.*, 2019, **489**, 875–882.
40 K. S. Ranjith and R. T. Rajendra Kumar, *RSC Adv.*, 2017, **7**, 4983–4992.
41 B. Subash, B. Krishnakumar, R. Velmurugan, M. Swaminathan and M. Shanthi, *Catal. Sci. Technol.*, 2012, **2**, 2319–2326.
42 B. Subash, B. Krishnakumar, R. Velmurugan, M. Swaminathan and M. Shanthi, *Catal. Sci. Technol.*, 2012, **2**, 2319–2326.
43 S. Dhanavel, E. A. K. Nivethaa, K. Dhanapal, V. K. Gupta, V. Narayanan and A. Stephen, *RSC Adv.*, 2016, **6**, 28871–28886.
44 Z. Xiong, L. L. Zhang, J. Ma and X. S. Zhao, *Chem. Commun.*, 2010, **46**, 6099–6101.
45 R. Sumathi, *Int. Res. J. Eng. Technol.*, 2016, **3**, 907–913.
46 R. Dadigala, R. Bandi, B. R. Gangapuram and V. Guttena, *Nanoscale Adv.*, 2019, **1**, 322–333.
47 A. Fouda, S. E.-D. Hassan, M. A. Abdel-Rahman, M. M. S. Farag, A. Shehal-deen, A. A. Mohamed, S. M. Alsharif, E. Saied, S. A. Moghanim and M. S. Azab, *Curr. Res. Biotechnol.*, 2021, **3**, 29–41.
48 M. R. Islam and M. G. Mostafa, *Appl. Water Sci.*, 2020, **10**, 119–129.
49 M. Noman, M. Shahid, T. Ahmed, M. B. K. Niazi, S. Hussain, F. Song and I. Manzoor, *Environ. Pollut.*, 2019, **254**, 1–36.
50 L. N. Du, S. Wang, G. Li, Y. Y. Yang, X. M. Jia and Y. H. Zhao, *Water Sci. Technol.*, 2011, **63**, 1531–1538.
51 C. I. L. Ebency, S. Rajan, A. G. Murugesan, R. Rajesh and B. Elayarajah, *Int. J. Curr. Microbiol. Appl. Sci.*, 2013, **2**, 496–505.
52 T. Ahmed, M. Noman, M. Shahid, M. B. K. Niazi, S. Hussain, N. Manzoor, X. Wang and B. Li, *Environ. Res.*, 2020, **191**, 110142.
53 R. C. Ngullie, S. O. Alaswad, K. Bhuvaneswari, P. Shanmugam, T. Pazhanivel and P. Arunachalam, *Coatings*, 2020, **10**, 500–514.
54 H. Wang, J. Bai, M. Dai, K. Liu, Y. Liu, L. Zhou, F. Liu, F. Liu, Y. Gao, X. Yan and L. Geyu, *Sens. Actuators, B*, 2020, **304**, 127287.
55 X. Gao, B. Yang, W. Yao, Y. Wang, R. Zong, J. Wang, X. Li, W. Jin and D. Tao, *Environ. Pollut.*, 2019, **1**, 1–35.
56 N. I. Md Rosli, S.-M. Lam, J.-C. Sin, I. Satoshi and A. R. Mohamed, *J. Environ. Eng.*, 2018, **144**, 04017091.

57 Q. Guo, L. Fu, T. Yan, W. Tian, D. Ma, J. Li, Y. Jiang and X. Wang, *Appl. Surf. Sci.*, 2020, **509**, 144773.
58 N. Kumaresan, M. M. A. Sinthiya, M. Sarathbavan, K. Ramamurthi, K. Sethuraman and R. R. Babu, *Sep. Purif. Technol.*, 2020, **244**, 116356.
59 B. B. Mulik, B. D. Bankar, A. V. Munde, P. P. Chavan, A. V. Biradar and B. R. Sathe, *Appl. Surf. Sci.*, 2021, **538**, 148120.
60 M. Ismael, *Chem. Phys. Lett.*, 2020, **739**, 136992.
61 P. Yang, J. Wang, G. Yue, R. Yang, P. Zhao, L. Yang, X. Zhao and D. Astruc, *J. Photochem. Photobiol., A*, 2020, **388**, 112169.
62 R. Uma, K. Ravichandran, S. Sriram and B. Sakthivel, *Mater. Chem. Phys.*, 2017, **201**, 147–155.
63 Q. Chen, H. Hou, D. Zhang, S. Hu, T. Min, B. Liu, C. Yang, W. Pu, J. Hu and J. Yang, *J. Photochem. Photobiol., A*, 2018, **350**, 1–9.
64 A. Elleuch, Z. Chaâbene, D. C. Grubb, N. Drira, H. Mejdoub and B. Khemakhem, *Ecotoxicol. Environ. Saf.*, 2013, **98**, 46–53.
65 R. G. Saratale, G. S. Ghodake, S. K. Shinde, S. K. Cho, G. D. Saratale, A. Pugazhendhi and R. N. Bharagava, *J. Environ. Manage.*, 2018, **223**, 1086–1097.